Electrical Engineering
https://doi.org/10.1007/s00202-024-02884-w

ORIGINAL PAPER

Performance improvement of grid-connected PV systems using modified Cuk-Landsman converter and hybrid PI controller strategy

E. Immanuvelbright[1] · R. Muthukumar[1]

Received: 30 July 2024 / Accepted: 27 November 2024

Abstract
The integration of photovoltaic (PV) system into the grid is increasingly important for sustainable energy solutions. This paper presents a novel approach to improve the performance of grid-connected PV by incorporating the modified Cuk-Landsman converter and a hybrid proportional integral (PI) controller strategy. The modified Cuk-Landsman converter is designed to effectively boost the output voltage of the PV panels, ensuring optimal power transfer and increased efficiency. The switching operation of this converter is further enhanced using a Hybrid Firefly and Swallow Swarm optimized-tuned PI controller that combines Firefly and Swallow Swarm techniques to fine-tune the parameters of the PI controller. This optimized PI controller demonstrates superior dynamic response and robustness in managing the power output of the PV system. Besides, to ensure stable battery voltage regulation and effective power management, a bidirectional DC to DC converter is incorporated. This converter facilitates efficient charging and discharging operations, thus maintaining optimal battery performance and extending its lifespan. A Recurrent Neural Network controller is employed to accomplish efficient grid synchronization, assuring accurate and reliable integration of the PV system with grid. The experimental and simulation outcomes confirm the effectiveness of the developed work, showing significant improvements in efficiency (96.8%), and THD (1.02%) when compared to other classical methods.

Keywords PV system · Modified Cuk-Landsman converter · Hybrid firefly and swallow swarm optimized (HFA-SSO) PI controller · RNN controller and battery

Abbreviations

PV	Photovoltaic
PI	Proportional integral
HFA-SSO	Hybrid firefly and swallow swarm optimization
GWO	Grey wolf optimization
PSO	Particle swarm optimization
ANN	Artificial neural network
GA	Genetic algorithm
IAE	Integral absolute error
SSO	Swallow swarm optimization
THD	Total harmonic distortion
DC	Direct current
VSI	Voltage source inverter
RNN	Recurrent neural network
SEPIC	Single-ended primary inductance converter
GA	Gradient adaptive
ACO	Ant colony optimization
P	Proportional
I	Integral
SOC	State of charge
WO	Whale optimization
AC	Alternating current
FPGA	Field programmable gate array
ISE	Integral of square error
FA	Firefly algorithm

✉ E. Immanuvelbright
immanuvelbright12@yahoo.com

[1] Department of Electrical and Electronics Engineering, Erode Sengunthar Engineering College, Perundurai, Erode 638057, India

1 Introduction

Grid-connected PV systems have become a pivotal component in the transition to cleaner energy, offering an efficient means of harnessing solar power and integrating it into the

Published online: 10 December 2024

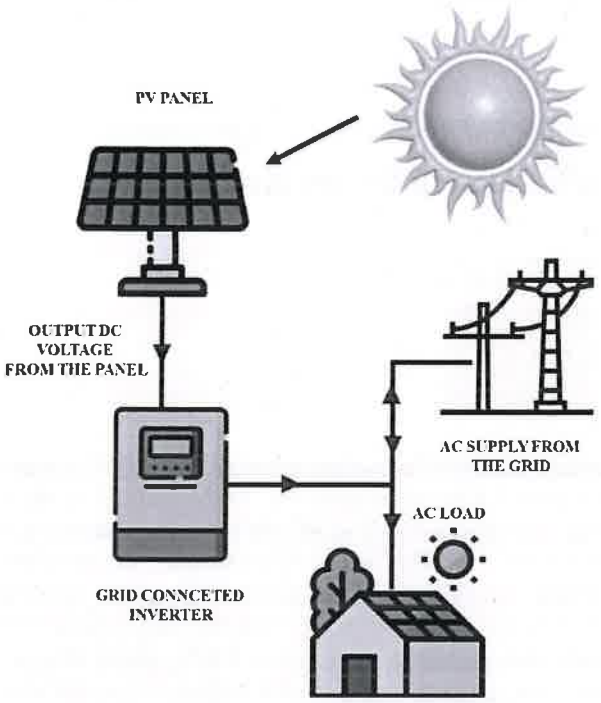

Fig. 1 Solar photovoltaic on grid system

existing electrical grid [1, 2]. However, the performance and reliability of these systems are often challenged by fluctuations in solar irradiance, temperature variations, and the nonlinear characteristics of PV modules [3]. To address these challenges, various control strategies and power electronics converters are employed to optimize the performance of grid-connected PV systems [4]. Among these, the DC-DC converter plays a crucial role in managing the power output of the PV system [5]. The different types of dc to dc converters are utilized for enhancing PV voltage. Boost [6], converters are simple and efficient for stepping up voltage but suffer from the high voltage stress and reduced efficiency. Buck-Boost [7], converter provide versatile voltage conversion, but have higher component stress and reduced efficiency. The Cuk converter [8], offers better input and output current characteristics but are complex and require more components. Similarly, the Single Ended Primary Inductance Converter (SEPIC) [9] enable for non-inverted output voltage and easy implementation, yet they are less efficient and have higher component count. Zeta [10] converter have similarities with SEPIC converter non-inverted output but are also less efficient and complex. Luo converter [11] have been proposed for PV systems. Figure 1 illustrates the structure of PV-connected grid system with AC load supply.

To alleviate these issues, hybrid converter topologies are proposed for balancing voltage stress, enhancing efficiency, reducing ripple, and improving overall performance. The hybrid converter topology presented in [12], uses a single power switch to enable continuous current mode function, reducing the voltage stress on regulated diodes and switches. However, with this design, the diode reverse recovery current predominates whenever working at higher voltages and currents, which raises the switching stress. A hybrid modified converter is presented in [13] for PV applications. This converter has good features including, minimized voltage stress for diodes and continuous input current with reduced ripples. But, this converter has low efficiency owing to its tough switching operation. A PV system using hybrid zeta-boost converter is proposed in [14], which attains maximum conversion efficiency lacking of multiple phases of capacitor and diode circuitry and the high-frequency transformer. However, this converter has increased complexity and also has increased components, resulting in more expensive. The hybrid converter presented in [15], which has maximum efficiency with increased voltage gain, thus making it appropriate for renewable applications especially for PV systems. However, this converter uses highly proficient components for circuit design, resulting in more expensive. Therefore, this work employs a novel Modified Cuk-Landsman converter for encountering the limitations of abovementioned converters. Table 1 represents the summary of classical methods advantages and disadvantages of PV-connected grid system.

In general, the classical PI controller [16] is used in DC to DC converters, limitations that hinders their effectiveness in improving switching operations. One major issue is their reliance on fixed parameters, which is not optimal across varying operating conditions, which is changes in input voltage. This leads to suboptimal performance, manifesting as increased settling time, overshoot, or steady-state error. Metaheuristic algorithms offers a robust solution to these problems by providing an adaptive and intelligent tuning mechanism for PI controller parameters. For example, Gradient Adaptive (GA) algorithm-tuned PI controller [17], Grey Wolf Optimization (GWO)-based PI controller [18], Whale Optimization (WO)-tuned PI controller [19], Ant Colony Optimization (ACO)-based PI controller [20] and Particle Swarm Optimization (PSO)-based PI controller [21] have been proposed for accomplishing the optimal performance in renewable source applications. These methods search for optimal or near-optimal parameter settings by mimicking natural processes and swarm intelligence, thus enhancing the controller's performance over a wide range of operating conditions. However, they have some own set of drawbacks. One major issue is computational complexity: these algorithms often require significant computational resources and time to find optimal solutions that is not achievable for real-time applications. Additionally, these algorithms can sometimes coverage to local optima rather than the global optimum, leading to suboptimal performance. Henceforth,

Table 1 Summary of existing survey on PV-connected grid system

Author [reference]	Methodology	Advantages	Disadvantages	THD%	Efficiency %
Jitendra Kumar Singh [2022]	Proportional Resonant (PR) controller	Fast reference tracking Easier implementation compared to other controllers	System needs fast convergence to maximize power transfer and creating challenges	1.93	95.7
Mohit Bajaj [2020]	Boost converter with APM controller	Handling wide range of input and output voltages	This require noise countermeasures	4	–
Haoyu Wang [2020]	Fuzzy Logic Controller	FLCs are robust to environmental changes and system uncertainties	It faces, tuning difficulty and computational complexity	–	93
Veramalla Rajagopal [2022]	DC-DC converter along with PI controller	Estimate solar grid currents to generate pulses for three leg converter	Systems face challenges in reliability, power quality, and performance	2	96
Kamrul Hasan [2020]	DC-DC buck boost converter	Achieve high efficiency by minimizing power losses in the switch, inductor, diode, and capacitor	High gain is limited, as efficiency doesn't support maximum gain	2.05	95.32

this paper presents an effectual hybrid FA-SSO-tuned PI controller to address these limitations by integrating these two FA and SSO algorithms, this method ensures a more balanced exploration and exploitation, resulting in more reliable and accurate for tuning PI control parameters.

The efficient grid synchronization is significant for the consistent and efficiency of power systems, which is accomplished deploying various controllers including PI [22] and Artificial Neural Network (ANN) controller [23]. PI controller has ability to provide a steady-state error correction, but it can't perform well under rapid changing conditions. ANN controller, on other hand, has the ability to handle the nonlinearities by learning from the grid operating conditions. Nonetheless, it prone to overfitting issues and has high computational cost. Therefore, RNN-based approach is employed in this paper to address these limitations by incorporating memory elements that captures the temporal dependencies in the gird's behavior. In this regard, the following are the primary contributions of the proposed research:

- Modified Cuk-Landsman converter is designed to enhance the stability and efficiency of the PV system by providing better voltage regulation and reducing power losses.
- To dynamically adjust the PI parameters, HFA-SSO approach improves the transient response, reduce overshoot, and enhance stability of the system.
- With the implementation of RNN-based controller, efficient grid synchronization is accomplished for PV-connected utility grid.

2 Proposed system description

A sophisticated grid-connected PV system enhanced with modern converter and control strategy is demonstrated in Fig. 2. The low voltage produced by the PV system is stepped up using a modified Cuk-Landsman converter. This converter is specially designed to handle the variable DC output from the PV system, ensuring it is boosted to a higher level suitable for further processing and utilization. The performance of proposed converter is significantly strengthened through the implementation of an optimized PI controller. This optimized PI controller employs hybrid Firefly and Swallow Swarm algorithms to fine-tune its parameters, ensuring precise and efficient voltage regulation, minimizing power losses, and improving the overall stability and response of the converter. To manage the energy efficiently, a battery system is integrated to preserve any surplus energy produced by the PV system. The regulation of this energy storage process is handled by a bidirectional battery converter, which allows for both charging and discharging operations. This bidirectional capability ensures that the battery storing the energy when

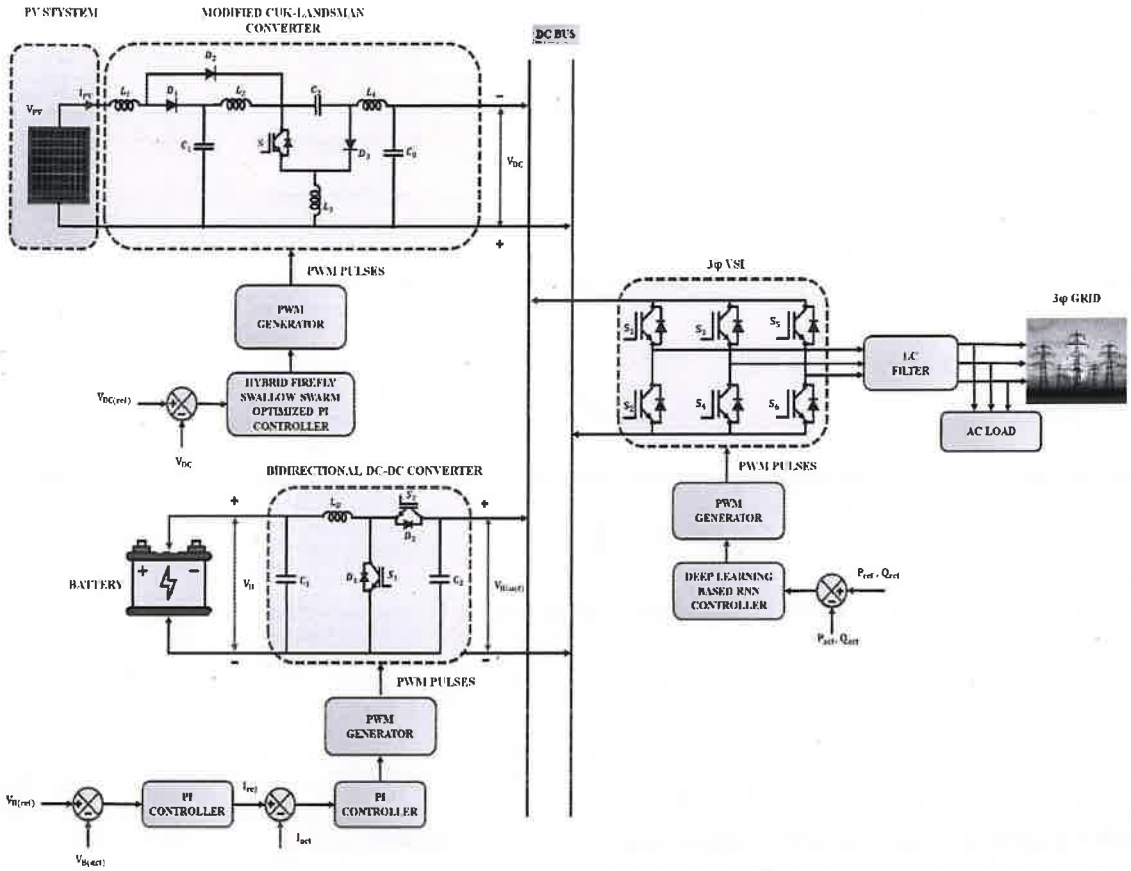

Fig. 2 Performance improvement of grid-connected PV system using hybrid optimized PI controller

excess power is available and supply power back to the system when needed, maintaining a balanced energy flow and optimizing the use of generated power.

Finally, to ensure that the generated power is effectively synchronized with the grid, a RNN controller is employed. The RNN controller excels in managing the dynamic and nonlinear nature of grid synchronization, adapting to fluctuations and changes in grid conditions. This deep learning-based controller assures the power from PV system is seamlessly integrated with the grid, maintaining stability and efficiency in power delivery to the end-users. The combination of these advanced technologies ensures a highly efficient, reliable, and robust grid-connected PV system. This enhanced performance contributes to the reliability and sustainability of grid-connected PV systems, making them more viable for widespread adoption in renewable energy applications.

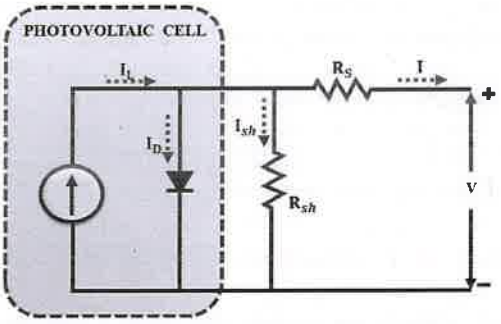

Fig. 3 PV cell

3 System modeling

3.1 PV system modeling

Generally, the irradiance and temperature have an influence on a PV module's operational point. The PV system model is illustrated in Fig. 3.

The basic current (I) equation for PV system is outlined below:

$$I = I_{\text{pvcell}} - I_{\text{ocell}}[exp^{\frac{(qv)}{aKT}} - 1] \quad (1)$$

$$I = I_{pv} - I_o\left[\exp^{\left(\frac{(v+R_s.I)q}{aV_k}\right)-1}\right] - (v + R_s.I)/R_p \quad (2)$$

where, the I_o is indicated by output current, $v_k \rightarrow kT/q$, q represents the electron charge I_{pv} is PV current, ideality coefficient is$a$, Boltzmann constant is indicated by$k$, the voltage across the diode is represented by$v$, temperature factor is T and R_p, R_s is represented by series and shunt resistance of PV panel. As the temperature and irradiance change, the amount of preserved power in the PV also changes, so the obtained Eq. (2) is,

$$I = I = I_{pv} - I_o\left[\exp^{\left(\frac{(v+R_s.I)q}{aV_kT.N_s}\right)-1}\right] - (v + R_s.I)/R_p \quad (3)$$

where N_s is the amount of PV array series, the output of panel is always poor due to the intermittent nature of PV system, this PV voltage further enhanced through the use of appropriate DC to DC converter that is explained in the following section.

3.2 Modeling of modified Cuk-Landsman converter

The output voltage of PV panel is strengthened using modified Cuk-Landsman converter. The Modified Cuk-Landsman Converter is indeed a suitable choice for integrating PV systems into the grid, particularly due to its specific advantages in high-gain applications. One of the primary benefits of this converter is its ability to achieve a higher output voltage gain while maintaining efficiency, which is critical for ensuring optimal power transfer from PV panels. This proposed converter is a novel approach designed to overcome the limitations of conventional converters while integrating their gainful features. Furthermore, the strong characteristics of the designed converter topology is continuous input current and lesser normalized value of power stresses on semiconductor. Meanwhile, the designed converter has maximum voltage conversion ratio with high efficiency, thus making it appropriate to implement in renewable applications especially for PV systems.

3.2.1 Working of the modified Cuk-Landsman converter

The proposed Modified Cuk-Landsman converter circuit diagram is showcased in Fig. 4. The working function of converter is splitted into two sections, Mode 1 and Mode 2 as discussed in detail in the section that follows. The operational states of developed converter are showcased in Fig. 5.

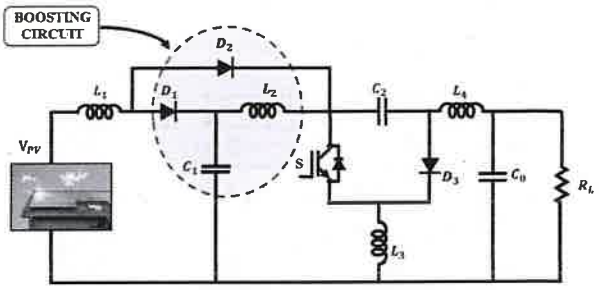

Fig. 4 Proposed modified Cuk-Landsman converter

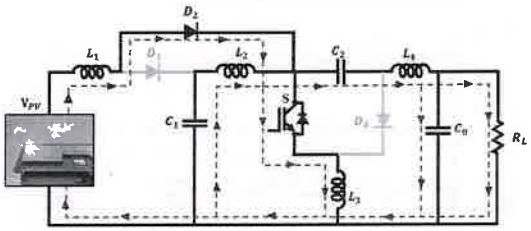

(a) Mode 1

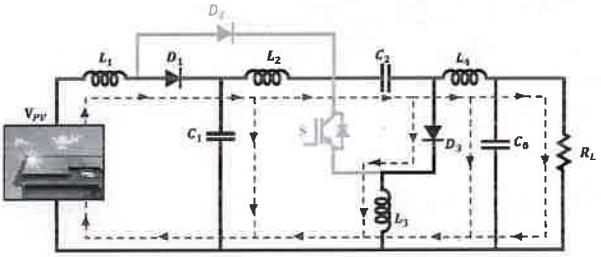

(b) Mode 2

Fig. 5 Operating modes

Similarly, the modified Cuk-Landsman converter timing diagram is indicated in Fig. 6.

Mode 1: $[\,0 - \boldsymbol{DT_s}]$

The proposed converter mode 1 operation is illustrated in Fig. 4a, this state is in between 0 and DT_s. Where, the switching frequency of the converter is represented by T_s and the duty factor of the converter is D. The controlled circuit is in active mode in this period of time. The diode D_2 is forward bias mode owing to the V_{PV} input supply. As seen in Fig. 4a, the diodes D_1 and D_3 are not conducting because of a reverse bias mode caused by capacitors C_1 and C_o, respectively. Capacitors C_1 and C_2 are energized by the inductors L_1, L_2,L_3 and L_4 correspondingly. The capacitor voltage slope is decreased owing to its discharging nature, while the current passing through the inductors is increased, then the load obtains the discharged energy of the capacitor C_o. Due to the OFF position, diode D_3 has a negative voltage across it and there is no electrical current passing through it.

Applying Kirchhoff's voltage law in mode 1,

$$V_{PV} - V_{L1} - V_{L3} = 0 \quad (4)$$

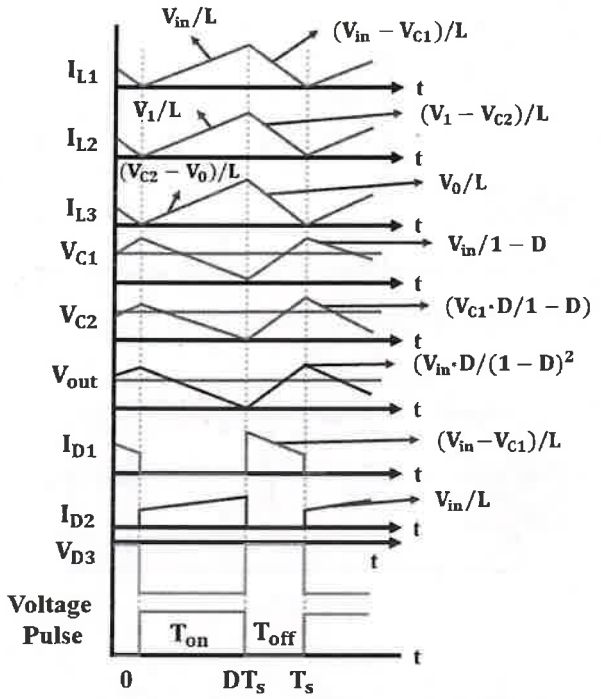

Fig. 6 Timing diagram of modified Cuk-Landsman converter

$$V_{C1} - V_{L2} - V_{L3} = 0 \tag{5}$$

$$V_{C1} - V_{L2} - V_{C2} - V_{L4} \tag{6}$$

$$V_{Co} = V_o = V_{RL} \tag{7}$$

Mode 2: $[DT_s - T_s]$

Mode 2 occurs between DT_s and T_s, the regulated device (switch) is in non-conducting mode throughout this time. Through diode D_1, input supply V_{PV} and inductor L_1 are discharged into capacitor C_1. Via diodes D_1 and D_3, the inductor L_1 and L_2 and the input supply V_{PV} are demagnetized and placed into capacitor C_2. Via diode D_3, the inductor L_3 is demagnetized and becomes a capacitor C_o. As seen in Fig. 4b, mode 2 is characterized by demagnetization of the four inductors L_1, L_2, L_3 and L_4 or a decrease in the current transformed through the three inductors. Four inductors L_1, L_2, L_3, L_4 and power source supply V_{PV} charge the three capacitors C_1, C_2 and C_o. As seen in Fig. 4b, the current passing through capacitors C_1, C_2 and C_o is increasing.

Applying Kirchhoff's voltage law in mode 2,

$$V_{PV} - V_{L1} - V_{C1} = 0 \tag{8}$$

$$V_{C1} - V_{L2} - V_{C2} - V_{L3} = 0 \tag{9}$$

$$V_{L4} - V_{Co} - V_{L3} = 0 \tag{10}$$

The dropped voltage over the regulated power switch S and the diodes D_1, D_2, D_3 are assumed as V_d for reducing the voltage conversion ratio complexity.

According to volt second balance law for inductor L_1 is,

$$\left.\begin{aligned}(V_{PV} - 3V_d)D + (V_{PV} - V_{C1} - 2V_d)(1 - D) = 0\\ V_{C1} = \left(\tfrac{V_{PV}}{1-D}\right) - 2V_d\left(\tfrac{1+D}{1-D}\right)\end{aligned}\right\} \tag{11}$$

Volt second balance law for inductor L_2,

$$\left.\begin{aligned}(V_{C1} - 2V_d)D + (V_{C1} - V_{C2} - 2V_d)(1 - D) = 0\\ V_{C2} = \tfrac{V_{C1}}{(1-D)} - \tfrac{2V_d}{(1-D)}\end{aligned}\right\} \tag{12}$$

Volt second balance law for inductor L_3,

$$\left.\begin{aligned}(V_o - V_{C2} - 2V_d)D + (V_o - 2V_d)(1 - D) = 0\\ V_o = DV_{C2} - 2V_d\end{aligned}\right\} \tag{13}$$

From Eq. (12),

$$V_o = \frac{D}{(1 - D)}V_{C1} - 2V_d\left(\frac{2 - D}{1 - D}\right) \tag{14}$$

From Eq. (11),

$$V_o = \frac{D}{(1 - D)^2}V_{PV} - 4V_d\left(\frac{D^2 - D - 1}{1 - D}\right) \tag{15}$$

The modified Cuk-Landsman converter voltage conversion ratio is represented in Eq. (15). Here the internal resistance of the elements assumed as neglected or zero, then the obtained Eq. (15) is,

$$V_o = \frac{D}{(1 - D)^2}V_{PV} \tag{16}$$

The identical voltage conversion range of the proposed modified Cuk-Landsman converter is indicated in Eq. (16). The switching operation of the proposed converter is optimally enhanced by using HFA-SSO-tuned PI controller, which is clearly explained in the following section.

3.3 Modeling of hybrid firefly-swallow swarm optimized PI controller

The Hybrid Firefly-Swallow Swarm Optimized (HFA-SSO) PI controller for enhancing the performance of a Modified Cuk-Landsman converter operates by first comparing the reference voltage $V_{dc(ref)}$ with the actual output voltage $V_{dc(act)}$ using a comparator to generate an error signal $e_{(t)}$. This error

Table 2 Parameter specifications for HFA-SSO algorithm

Parameter	Description	Value
Population SIZE (N)	Number of fireflies and swallow swarm agents in the population	30
Max iterations	Maximum number of iterations for the optimization process	50
Step size (s)	Step size for the random walk used in the optimization process	0.1
Swarm size (S)	Number of agents in the Swallow Swarm Optimization part of the hybrid algorithm	20
Food source (FS)	Number of food sources to be considered in the Swallow Swarm Optimization	5
Exploration rate (ER)	Probability of exploration versus exploitation during the optimization process	0.7
Exploitation rate (XR)	Probability of exploitation during the optimization process	0.3

signal is fed into the PI controller that adjusts its output based on the proportional (P) and integral (I) terms to minimize this error over time. Here, the PI controller parameters K_p, K_i, are tuned through this hybrid optimization process, which is analyze the optimized values and impacts the key performance metrics such as settling time, overshoot and error minimization. The HFA-SSO algorithm optimizes the PI controller parameters by combining the strengths of firefly and swallow swarm optimization techniques to find the optimal gain values, enhancing the dynamic response and stability of the converter. The output of the PI controller is then used to modulate the duty cycle of the PWM signal, which drives the switch in the converter. Using PWM duty cycles, the PI controller regulates the converter's output voltage to match the desired reference voltage, ensuring efficient and stable operation. The flowchart representation of HFA-SSO-tuned PI controller is denoted in Fig. 7. The parameter specifications of HFA-SSO are provided in Table 2.

3.3.1 PI controller

The steady-state error is eliminated and the necessary forward gain is decreased by including integral feedback. The proportional speed controller is swapped out for a PI controller in order to acquire this integral component. Equation (17) states the expanded term of the PI controller, where

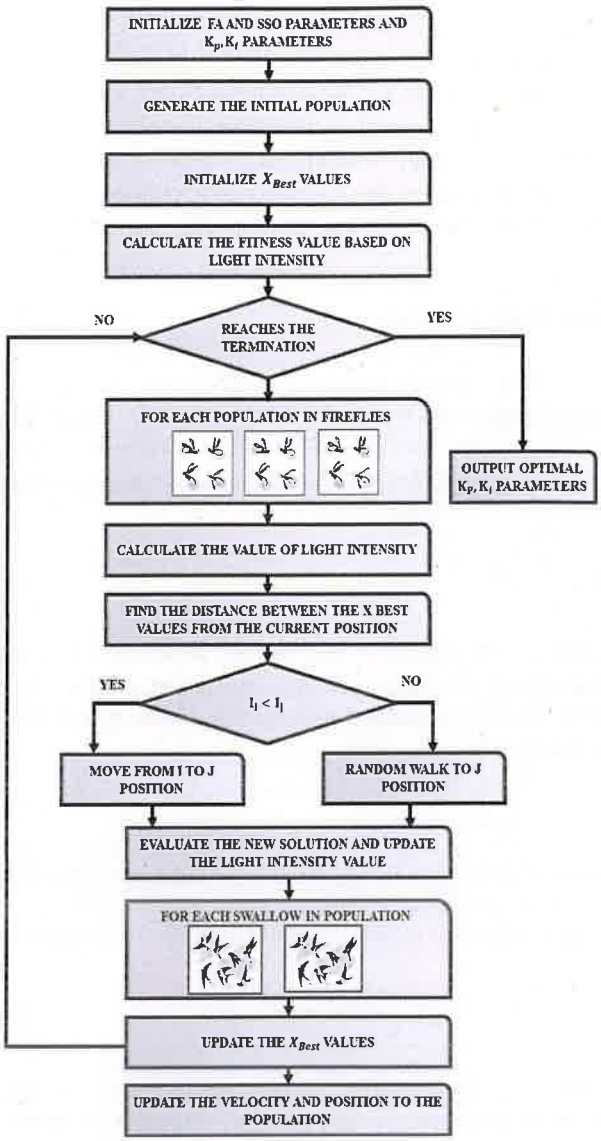

Fig. 7 Flowchart of HFA-SSO-tuned PI controller

k_P the proportional is gain and k_i is the integral gain.

$$u(t) = k_P e(t) + k_i \int e(t)dt \tag{17}$$

The expression (18) is transformed into Eq. (19) utilizing the Laplace transform

$$U(s) = k_P E(s) + \frac{k_i E(s)}{s} \tag{18}$$

PI regarding the time constraints is expressed in Eq. (18)

$$U(s) = k_P[1 + \frac{1}{\tau_i}]E(s) \tag{19}$$

where $k_i = \frac{k_P}{\tau_i} and k_P = k_d/\tau_i$

The steady-state error is decreased and error signal is more finely controlled by the proportional and integral terms. When k_P and k_i parameters are precisely tuned for a closed-loop control system, the settling time improves and the rise time somewhat decreases. Currently, a PI controller has been put into place for enhancing control performance of the system.

3.3.2 Firefly algorithm

The FA is a swarm intelligent metaheuristic method that draws inspiration from firefly behavior in their natural surroundings. Equation (20) indicates that the intensity of light I diminishes with the square of the distance r in accordance with the inverse square law.

$$I \propto \frac{1}{r^2}, I = \frac{1}{r^2} \tag{20}$$

where r is the separation between two fireflies and I is the intensity of the light. A firefly's attractiveness in a given environment is correlated with the light intensity I, which is determined by Eq. (21),

$$\beta(r) = \beta_{0e^{-\gamma r^2}} \tag{21}$$

where γ is the light absorption rate and β represents attraction at $r = 0$. The Euclidean distance, represented by Eq. (22) is used to determine the distance between firefly i and firefly j.

$$r_{ij} = ||X_i - X_j|| = \sqrt{\sum_{k=1}^{d} (xik - xjk)^2} \tag{22}$$

where r_{ij} is the separation among a pair of fireflies, X_i and X_j, with coordinates xik and xjk, and d is the firefly's dimension. As a result, according to Eq. (23), a less bright firefly i moves because it is drawn to a brighter firefly j that is more appealing.

$$X_i = X_i + \beta o e^{-\gamma r_{ij}^2} \left(X_j - X_i\right) + \propto \varepsilon_i \tag{23}$$

where $\propto$ is a randomized factor and ε_i is a random number from a Gaussian distribution.

3.3.3 Swallow swarm optimization

Recently, an innovative framework based on swarm intelligence called SSO has been developed to mimic the actions of swallow swarms. PSO and SSO have some characteristics, but they also differ significantly in several ways. The optimization process starts with a randomly generated initial population of particles that are modified throughout time. Every swallow that reaches an extreme point communicates to the others that it has arrived with a unique sound. That particle gets the Head Leader, HL^k, while that position is optimal in intended space. The particle is selected as a local leader or LL^k, if it moves into a favorable (but not optimal) position in relation to its surrounding particles. If not, the particle needs to move within the search space since it is an exploration one. By combining a varied velocity VHL_i^{k+1} to the present location X_i^k, taking into account VLL_i^{k+1} (particle of varied velocity vector toward Head Leader) and VLL_i^{k+1} (particle varied velocity vector toward Local Leader), a new location of the pioneer particles, X_i^{K+1} is produced, which is mathematically modeled as follow as,

$$X_i^{K+1} = X_i^k + V_i^{K+1}$$

$$V_i^{k+1} = VH_i^{k+1} + VLL_i^{k+1}$$

$$\begin{aligned} VHL_i^{k+1} &= VHL_i^k + \propto_{HL} \text{rand}()(X\text{best}_i^k - X_i^k) \\ &\quad + \beta_{HL} \text{rand}()(HL^k - X_i^k \end{aligned}$$

$$\begin{aligned} VLL_i^{k+1} &= VLL_i^k + \propto_{LL} \text{rand}()(X\text{best}_i^k - X_i^k) \\ &\quad + \beta_{LL} \text{rand}()(LL^k - X_i^k) \end{aligned} \tag{24}$$

whereas $rand()$ is a randomized values that consistently dispersed in (0, 1)$\propto_{HL}$,β_{HL} $\propto_{LL}$ and β_{LL} are acceleration control factors that are automatically determined.

While particles additionally perform exploration, wandering particles $o_{(i)}$ are independent of the local and head leaders. It is simply displace, moving forth and back in relation for their prior places through a randomized portion of permitted phase that is determined by the intended variables' lower and upper bounds, which is:

$$o_i^{k+1} = o_i^k + \left[\text{rand}(\{-1,1\}) \times \frac{\text{rand}(\min, \max)}{1 + \text{rand}()}\right] \tag{25}$$

3.3.4 Hybrid FA-SSO-tuned PI controller

The selection of the HFA-SSO-tuned PI controller for the hybrid PI controller is driven by its unique advantages in terms of convergence speed, accuracy, and adaptability to complex control environments. Unlike GA and PSO, the hybrid Firefly-Swallow Swarm approach combines the global exploration abilities of the Firefly Algorithm with the local search strengths of Swallow Swarm Optimization. This combination allows the controller to efficiently balance exploration and exploitation, achieving a more precise and stable optimization of the PI controller parameters. Usually, the FA often suffers from premature convergence and gets trapped in local optima, especially in complex system.

The SSO method is introduced to mitigate these issues by incorporating a swallow depth of field in the swarm 's movement, allowing for a more refined and balanced exploration and exploitation process. By combining the SSO principles with the FA's attraction mechanism, the HFA-SSO technique achieves a more robust optimization process, enhancing solution accuracy and convergence speed while effectively avoiding local optima traps. In this research the HFA-SSO algorithm is implemented for optimizing the parameters of PI controller. Pseudocode for HFA-SSO-tuned PI controller is illustrated below.

Pseudocode for HFA-SSO tuned PI controller

Input: *Population size, maximum iterations* K_p, K_i *parameter values, objective function*
Output: *Best* K_p *and* K_i *values*
Begin
Randomly initialize each $X_{firefly}$
Calculate fitness value;
For $i = 1$ *to* n;
For $i = 1$ *to* n;
Evaluate fitness function and get the current best solution;
if *current value of* $X_{firefly}(i).Cost <= BestSolution.Cost$ *Update the current* $X_{firefly}$ (i) *as the best solution;*
Best Solution $= X_{firefly}(i)$;
end if
end for
while maximum iteration (MaxIt) limit is not reached
for $i = 1$ *to* n;
if $X_{firefly}$ (j) < $X_{firefly}$ (j) *using Eqs.* (21) *and* (22);
Move $X_{firefly}(i)$ *towards* $X_{firefly}(j)$ *using Eqs.* (21) *and* (22);
if *newsolution* $<=$ $newX_{firefly}(i)$;
$new.X_{firefly}(i)$ *becomes the new solution;*
if $new.X_{firefly}(i).Cost <= BestSolution.Cost$;
Update $new.X_{firefly}(i)$ *as the new solution;*
end if
end if
end if
Randomly initialize $X_{SSO}(i) \leftarrow new.X_{firefly}(i)$;
determine the personal best and global best position of each particle X_{SSO} (i);
Calculate X_{SSO} (i) *fitness value us ;*
if X_{SSO}(i) $Cost <= newX_{firefly}$ (i).$Cost$
$X_{best} \leftarrow X_{SSO}$ (i);
else if new X_{SSO}(i) *fitness value is smaller than overall best fitness value, update the new value as the global best*
$X_{bset} \leftarrow X_{SSO}$ (i); *Update velocity and coordinates updating using Equation* (25);
end if
end if
end for
end for
end while
End

Advantages of the hybrid FF-SSO-tuned PI controller include improved convergence speed, ensuring real-time applicability. The method enhances robustness against dynamic system changes, maintaining optimal performance even under varying load conditions and input voltages. Additionally, the hybrid approach mitigates the risk of local optima, ensuring that the controller parameters are set to the best possible values for the given system. This leads to superior transient response, reduced overshoot, improved stability, and overall enhanced performance of the modified Cuk-Landsman converter.

3.3.5 Closed loop and open loop stability analysis for modified Cuk-Landsman converter

Considering the proposed converter and its output filter as a system that requires a controller to be established. The system's dynamic behavior is described by the following nonlinear equations:

$$u_i.a.V_{dc} = R_f i_{f,i} + L_f \frac{di_{f,i}}{dt} + v_{cf,i} \tag{26}$$

$$i_{f,i} = C_f \frac{di_{cf,i}}{dt} + i_{T,i} \tag{27}$$

The closed-loop optimum nonlinear resilient controller based on state feedback is used for developing u. Assuming the state vector $x(t)$ for each system stage is expressed as follows:

$$x_i(t) = \left[v_{cf,i}(t) i_{f,i}(t)\right]^T \tag{28}$$

where $v_{cf}(t)$ represents the initial voltage across the AC filter capacitor, $i_f(t)$ is the current running through the filter inductor L_f, and T is the transposition operator. The system's corresponding circuit can be expressed using the state space equation of,

$$\dot{x}_i(t) = Ax_i(t) + B_1 u_{c,i}(t) + B_2 i_{T,i}(T) \tag{29}$$

where,

$$A = \begin{bmatrix} 0 & \frac{1}{C_f} \\ -\frac{1}{L_f} & -\frac{R_f}{L_f} \end{bmatrix} B_1 = \begin{bmatrix} 0 \\ a.\frac{V_{dc}}{L_f} \end{bmatrix} B_2 = \begin{bmatrix} -\frac{1}{C_f} \\ 0 \end{bmatrix} \tag{30}$$

In Eq. (29), $uc(t)$ indicates the continuous time variation of the switching function u, while i_f reflects the effects of network load changes on the system, which are considered to cause a disturbance for the controller.

In control mechanisms, the ideal values for each control variable need to be determined under steady-state circumstances. However, it is difficult to discern the reference for i_f in (28). However, it is desired to have low frequencies. Instead of employing i_f as a control parameter, the high-frequency components ($\overset{\vee}{i}_f$) might be utilized in the control system. In accordance with this presumption, $\overset{\vee}{i}_f$ can be expressed and generalized in Laplace realm as,

$$\overset{\vee}{i}_f(s) = \frac{s}{s+a} i_f(s) = \left(1 - \frac{a}{s+a}\right) i_f(s) = i_f(s) - \widehat{i_f}(s) \tag{31}$$

The high-pass filter's cut-off frequency is a and its low-frequency elements are determined by, $\overset{\vee}{i}_f$.

$$\widehat{i_f}(s) = \frac{a}{s+a} i_f(s) \tag{32}$$

Equation (32) can be represented in differential mathematical form as:

$$\frac{d\widehat{i_f}(t)}{dt} = a\left(i_f(t) - \widehat{i_f}(t)\right) \tag{33}$$

Presently let's establish an additional state vector for the entire system, including $\overset{\vee}{i}_f$, as,

$$x_i'(t) = \left[v_{cf,i}(t) i_{f,i}(t) \widehat{i_{f,i}}(t)\right]^T \tag{34}$$

In this situation, the system is described by an updated space expression,

$$\dot{x}_i'(t) = A' x_i(t) + B_1' u_{c,i}(t) + B_2' i_{T,i}(t) \tag{35}$$

where,

$$A' = \begin{bmatrix} 0 & \frac{1}{C_f} & 0 \\ -\frac{1}{L_f} & -\frac{R_f}{L_f} & 0 \\ 0 & \alpha & -\alpha \end{bmatrix} B_1' = \begin{bmatrix} B_1 \\ 0 \end{bmatrix} B_1' = \begin{bmatrix} B_2 \\ 0 \end{bmatrix} \tag{36}$$

In the discrete-time domain, Eq. (35) is expressed as:

$$x_i'(k+1) = F x_i'(k) + G_1 u_{c,i}(k) + G_2 i_{T,i}(k) \tag{37}$$

where,

$$F = e^{A'T},\ G_1 = \int_0^{T_s} e^{A't} B_1' dt,\ G_2 = \int_0^{T_s} e^{A't} B_2' dt \tag{38}$$

Fig. 8 Bode plot

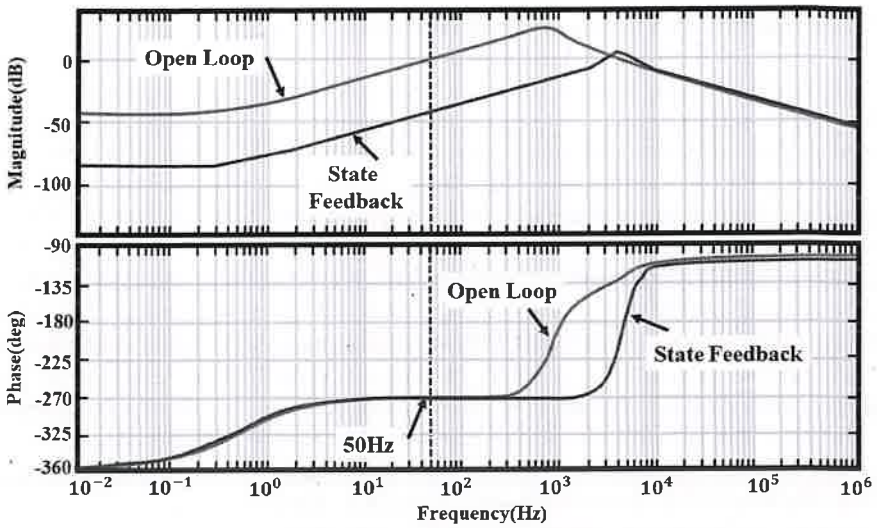

T_s represents the sample time. Using a proper state feedback control law, it is possible to estimate $u_c(k)$ from (37).

$$u_{c,j}(k) = -K[x_i'(k) - x_{ref,i}'(k)] \tag{39}$$

K is a gain matrix, and $x_{ref,i}'(k)$ is the required state vector for (34), in discrete-time systems mode. To attain stabilized output voltage, the proposed converter used a state feedback control system. The controller expression can be stated as follows:

$$\begin{aligned} u_i.a.V_{dc} &= v_{cf,ref,i} - K\left(X_i' - X_{ref,i}'\right) \\ &= v_{cf,ref,i} - k_1\left(v_{cf,i} - v_{cf,ref,i}\right) - k_2(i_{f,i} \end{aligned} \tag{40}$$

where $K = [k_1 k_2]$ is the gain matrix in (39). Combining (40) in (26) and expressing that in the Laplace domain yields the equation:

$$\begin{aligned} &v_{cf,i}(s)\left[L_f C_f s^2 + R_f C_f s + 1\right] + I_{T,i}(s)\left[L_f s + R_f\right] \\ &= V_{cf,ref,i}(s)[k_1 + 1] - k_1 V_{cf,i}(s) - \frac{k_2 s}{s+a} I_{f,i}(s) \end{aligned} \tag{41}$$

From (41), the variables of the Thevenin analogue circuit of the proposed converter and filter, comprising the constructed state feedback control, are given as,

$$\boldsymbol{V_{cf,i}(s) = G_1(s)V_{cf,ref,i}(s) + G_2(s)I_{T,i}(s)} \tag{42}$$

Frequency domain behavior is frequently used to compare the effectiveness of state feedback control and open loop transfer function in the Modified Cuk-Landsman Converter and filter system. Figure 8a and b show the Bode diagrams for $G_1(s)$ and $G_2(s)$). In Fig. 8a, it shows that at the frequency

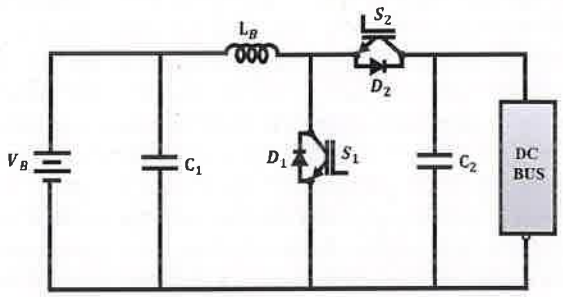

Fig. 9 Bidirectional DC to DC converter

band significance (i.e., 50 Hz), $G_1(s)$ has the characteristic of a gain of unity with zero angle. The significant value integrates network load and i_T change impacts into the converter operation. Appropriate layout of state feedback gains can effectively lower this size. It should be noticed that G2 $G_2(s)$ s) is relatively inductive at 50 Hz.

3.4 Modeling of bidirectional DC-DC converter

Energy conversion in the battery system depends on the bidirectional flow of electrical energy. To perform this, the control system makes use of a DC to DC current reversing chopper. Figure 9 shows the configuration of the converter that is being considered.

There are two regulated switches, an inductor, and a filter capacitor in the DC/DC converter. As a hybrid of a step down chopper and a step up chopper, the converter is a combination of the two fundamental chopper circuits. In addition to power mode operation when charging the battery, the DC/DC converter can also function as a regeneration mode when draining the battery.

3.5 Grid synchronization using RNN controller

Grid synchronization, power quality and active and reactive power regulation essentially rely on a grid-tied inverter producing the appropriate reference current waveform and injecting it into the electrical grid. The control approach is applied to the evaluation of harmonic fundamental components. Therefore, the design of the proposed strategy heavily relies on the following empirical relations. This synthetic dynamic load current and harmonic characteristics relevant to grid synchronization, allowing the RNN to train on a range of scenarios that represent the conditions encountered in grid-tied inverter operations. Equation (43) expresses the general equation of the current value on the load side. The basic formula and kth harmonic are both included in this equation. Equation (44) is the modified form of Eq. (43). There equations are particularly essential in modeling the current waveform on the load side, incorporating both fundamental and harmonic components. The RNN was trained using data synthesized from these equations, representing various harmonic scenarios and grid conditions. Equation (45) helped derive the phase and magnitude of the harmonics, ensuring the RNN could accurately interpret and respond to each component's behavior. Additionally, the measured error value, defined in Eq. (46), provided the loss function for the RNN during training, guiding the optimization of network parameters by minimizing the discrepancy between the predicted and actual current values.

$$i_L(t) = \sum_{k=1}^{N} I_{LK} \sin(k\omega t + \phi_k) \tag{43}$$

$$i_L(t) = \sum_{k=1}^{N} A_K \sin(k\omega t + B_k \cos(k\omega t) \tag{44}$$

$$I_{LK} = \sqrt{A_k^2 + B_k^2} \text{and} \theta_k = tan^{-1}\left(\frac{B_k}{A_k}\right) \tag{45}$$

where, $A_k = I_{LK} \cos\theta_k$ and $B_k = I_{LK} \sin\theta_k$

Equation (45) is used for determining the kth harmonic's phase and magnitude. In the present study, RNN is used to measure the dynamic load current related to various harmonics. The measured error value is represented in Eq. (46).

$$e(t) = \sum_{k=1}^{N} A_K \sin(k\omega t + B_k \cos(k\omega t) - i_{LK(t)} \tag{46}$$

RNN controller generates precise reference currents, enhancing the performance of power converters and ensuring efficient power delivery. Their adaptability to changing grid conditions, coupled with their ability to learn and predict future state.

For parameter optimization, the RNN training process leveraged the following key parameters:

1. Learning Rate: Set at 0.001 to balance the speed and stability of convergence.
2. Optimizer: Adam optimizer was used due to its adaptive learning rate and ability to handle sparse gradients, which is useful in time-series predictions like those required in grid synchronization.
3. Batch Size: A batch size of 32 was selected to enable efficient gradient calculations while maintaining computational feasibility.
4. Epochs: Training ran over 100 epochs, providing sufficient iterations for convergence without overfitting.
5. Hidden Layers and Units: The RNN architecture used 2 hidden layers, each with 64 units, providing the capacity needed for capturing complex temporal patterns without excessive computational demands.

These parameters were fine-tuned through trial and error, guided by the performance on the validation set created from the synthetic dataset, aiming for minimal prediction error and high fidelity in generating reference currents aligned with grid requirements.

4 Results and discussion

This work proposes an innovative hybrid optimized PI controller along with DC to DC converter for enhancing the performance of grid incorporated PV systems. The output PV voltage is increased through the application of Modified Cuk-Landsman converter, which attains high conversion ratio with maximum efficiency. The converter switching operation is improved with superior dynamic performance using hybrid FF-SSO-tuned PI controller. To store the excess energy from the PV panel battery is utilized, the battery voltage is regulated by PI controller. An effectual grid synchronization is achieved by RNN controller, thus minimized THD with high quality power with is supplied to grid as well as AC load. The proposed work efficacy is verified and validated through MATLAB/Simulink platform. The obtained simulation results for proposed hybrid optimized PI controller are discussed below. Table 3 showcases the parameters requirements of the proposed work.

4.1 Test case 1: constant temperature and constant intensity

Figure 10 represents the input and output waveforms of a solar power system under steady operating conditions. The solar temperature remains constant at 35 °C, ensuring stable thermal conditions for the system. Meanwhile, the solar intensity waveform is stable at 1000 W/m^2, providing a consistent amount of energy to the system. The input DC voltage

Table 3 Parameter specifications

Parameters	Values
Solar PV System	
Open circuit voltage	37.25 V
Short circuit current	8.95 A
Series-connected solar PV cell	33
Parallel-connected solar PV cell	11
Maximum power Voltage	29.95 V
Maximum current	8.35 A
Modified Cuk-Landsman Converter	
Switching frequency	10 kHZ
L_1, L_2, L_3, L_4	1 mH
C_1	$4.7\mu F$
C_o	$2200\mu F$

is maintained at a constant 100 V, ensuring a steady electrical supply, while the input DC current remains steady at 99A after 0.6 s, resulting in a stable flow of electrical current into the system. These consistent parameters suggest that the system operates under controlled conditions, optimizing energy conversion and performance.

Figure 11 shows the proposed converter output voltage and current waveforms, demonstrates the output voltage remains stable at 600 V maintained at 0.1 s. Similarly, the output current is steady at 10A, with a constant flow maintained over the 0.1 s period. These stable voltage and current conditions indicate that the DC-DC converter is efficiently regulating the power output, ensuring consistent performance during the time.

Figure 12 depicts the input and output power waveforms, where both the input and output power remain stable power flow over a 0.6 s period. This indicates a consistent power flow with minimal fluctuations, suggesting that the system is maintaining efficient energy conversion.

4.2 Test case 2: varying temperature and constant intensity

Figure 13 shows the solar input and output waveforms, that the solar temperature varies with a peak at 35 °C reached within 0.4 s, while the solar intensity remains constant at 1000 W/m^2. The input DC voltage waveform shows a peak at 100 V over a 0.4 s period, while the input DC current is stable and maintained at 98A for a duration of 0.6 s. This indicates that despite the variations in temperature, the solar intensity and electrical input conditions are stable, ensuring consistent power delivery to the system.

Figure 14 illustrates the developed converter output voltage and current waveforms. After 0.1 s, the output voltage stabilizes at 600 V, maintaining a constant voltage flow thereafter. Similarly, the output current reaches a steady value of 10A after 0.1 s and continues with a constant flow. These stable voltage and current conditions indicate that the developed converter is operating efficiently, with both the voltage and current remaining steady over time.

Figure 15 shows the input and output power waveforms from the PV system. The input power remains constant after

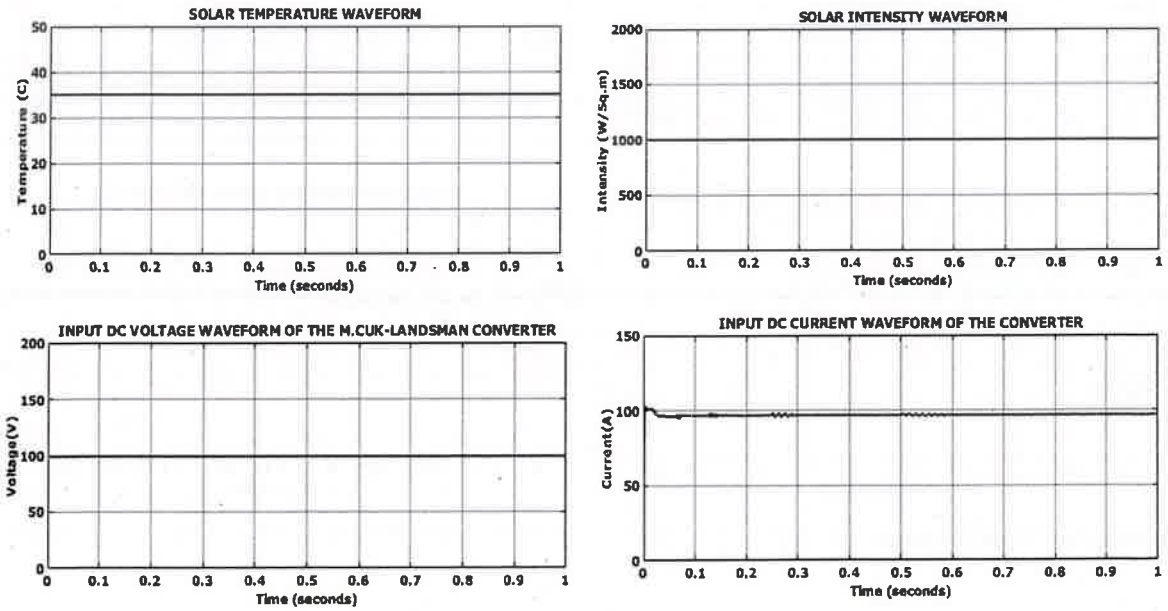

Fig. 10 Solar input and output waveform

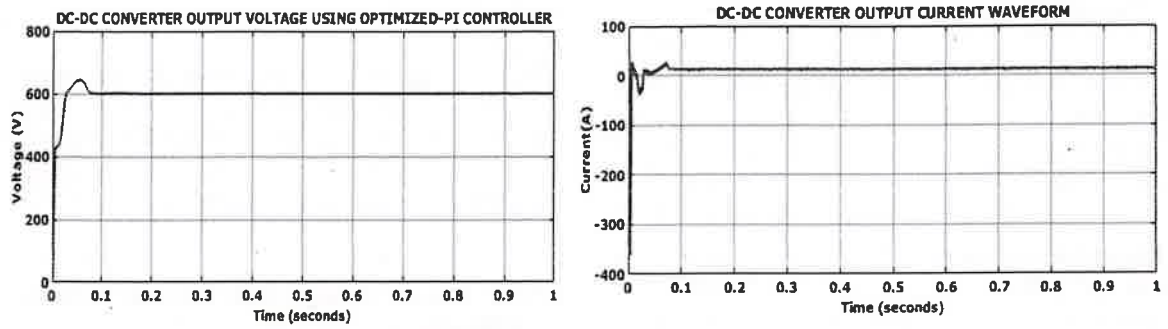

Fig. 11 Designed converter output voltage and current waveform

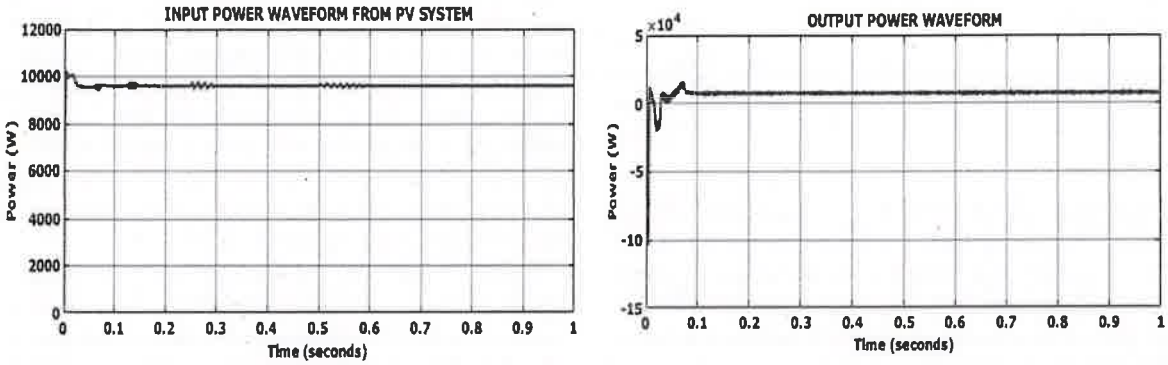

Fig. 12 Input and output power waveform

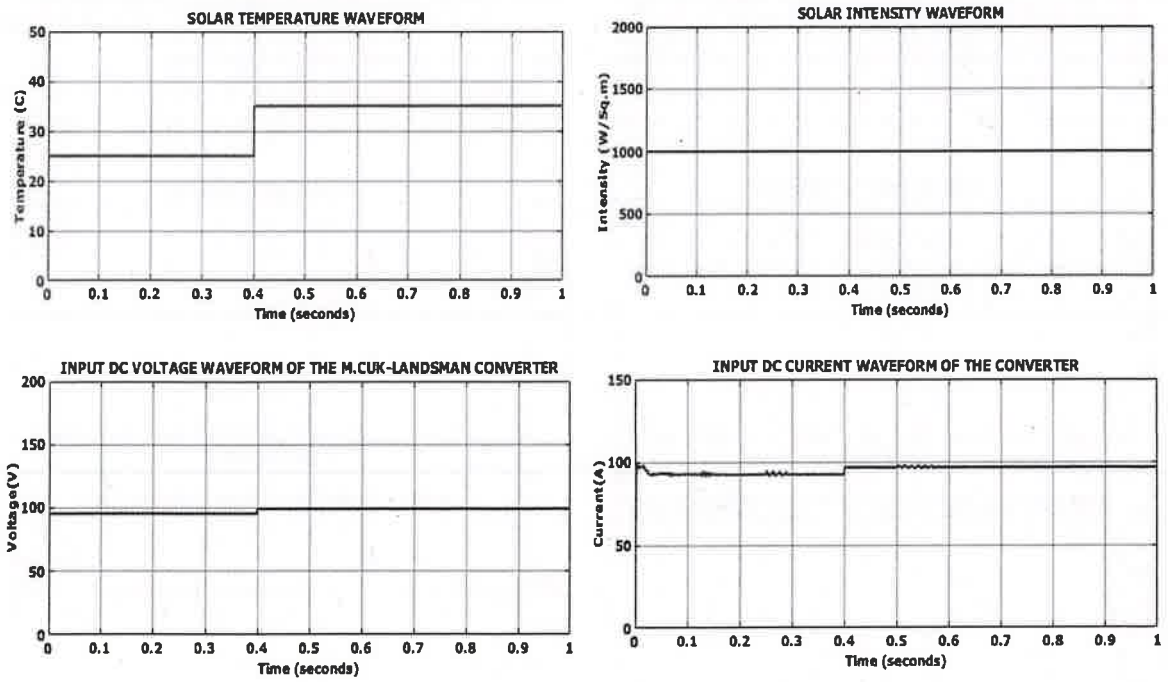

Fig. 13 Solar input and output waveform

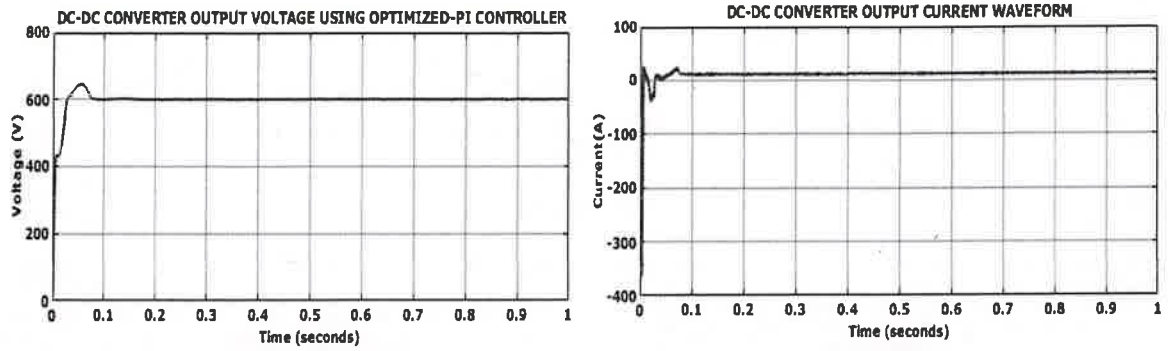

Fig. 14 Designed converter output voltage and current waveform

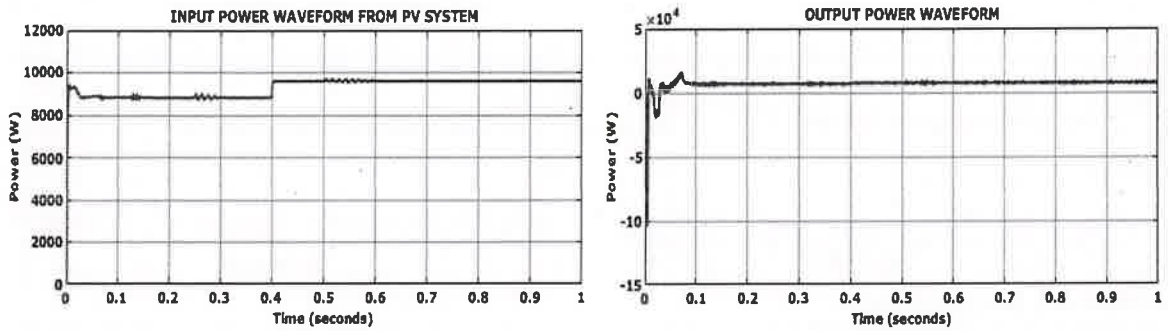

Fig. 15 Input and output power waveform from PV system

0.6 s, indicating a steady power flow into the system. In contrast, the output power exhibits some fluctuations over the time period, reflecting variations in the energy conversion.

4.3 Test case 3: constant temperature and varying intensity

Figure 16 presents the solar input and output waveforms, illustrates the solar temperature starts steady at 35 °C, while the solar fluctuates varying intensity, then its stabilizing a peak of 1000 W/m^2 at 0.7 s. The input voltage increases and peaks at 100 V after 0.7 s, followed by a steady state. Similarly, the input current reaches its peak of 98A within the same 0.7 s period and then maintains a constant flow. These dynamics illustrate how the system adapts to varying solar conditions while stabilizing after the initial fluctuations.

Figure 17 shows the DC-DC converter output voltage and current waveforms, that the output voltage maintains a constant flow at 600 V after 0.1 s and the output current increases and stabilizes at 10A after 0.7 s, continuing with a steady current flow. This behavior indicates that the converter efficiently regulates the voltage and current, providing a stable output over time.

Figure 18 illustrates the input and output power waveforms from the PV system, where both the input and output power initially fluctuate. After 0.7 s, the power flow stabilizes, with both the input and output power maintaining a steady flow. This indicates that the system has reached a stable operating condition after the initial variations in power output.

The operational characteristics of battery waveform are depicted in Fig. 19, here the obtained battery current, voltage and State of Charge (SoC) waveforms have maintained consistent values of $120V$, $2A$ and 60% correspondingly. Maintaining a 60% SoC involves careful regulation of the battery's discharge and charge cycles. The voltage waveform remains stable, the current waveform oscillates around $2A$ with small pulses indicating corrective charges and discharges, and the SoC waveform shows minor deviations around the 60% SoC. These waveforms together illustrate the system's efforts to keep the battery at a constant SoC, ensuring optimal performance and longevity. This controlled environment is crucial for applications requiring consistent battery performance and reliability.

The output waveforms of the three-phase grid voltage, current and inphase (which represents the R phase) waveforms are indicated in Fig. 20. To regulate the steady grid voltage the PI controller is implemented, thus the constant grid voltage $415V$ is maintained. Similarly the current value becomes consistent $12A$ and the grid current and voltage inphase waveform is seen in Fig. 20. Before, grid synchronization

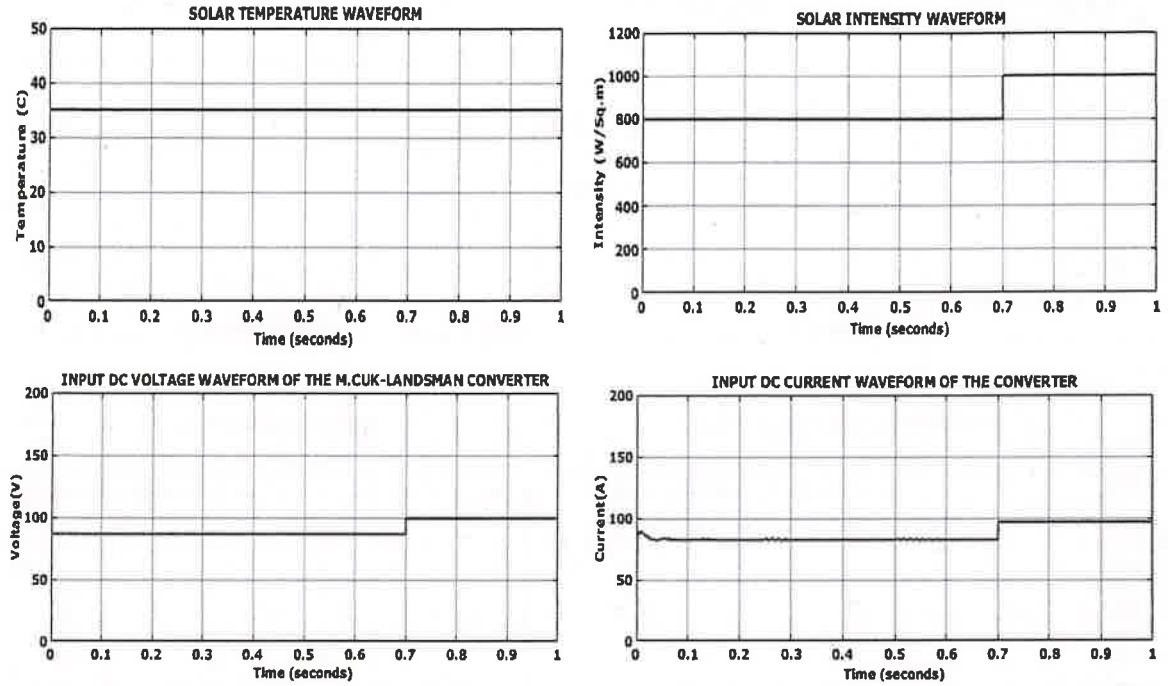

Fig. 16 Solar input and output waveform

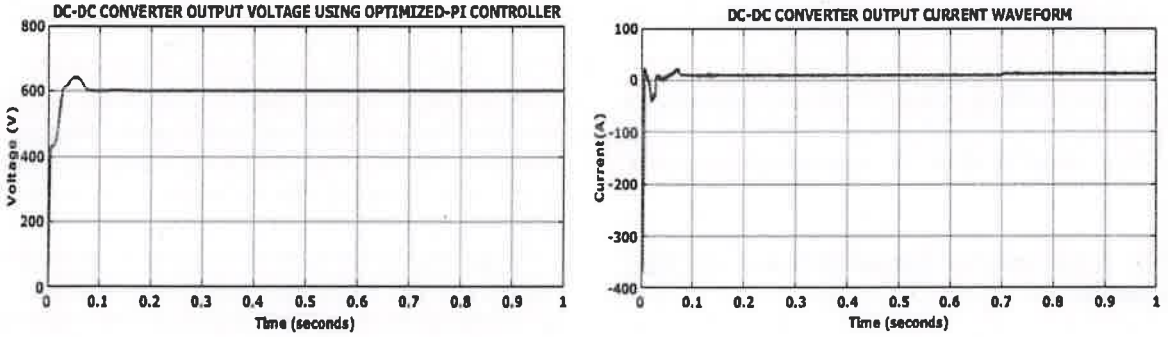

Fig. 17 Designed converter output voltage and current waveform

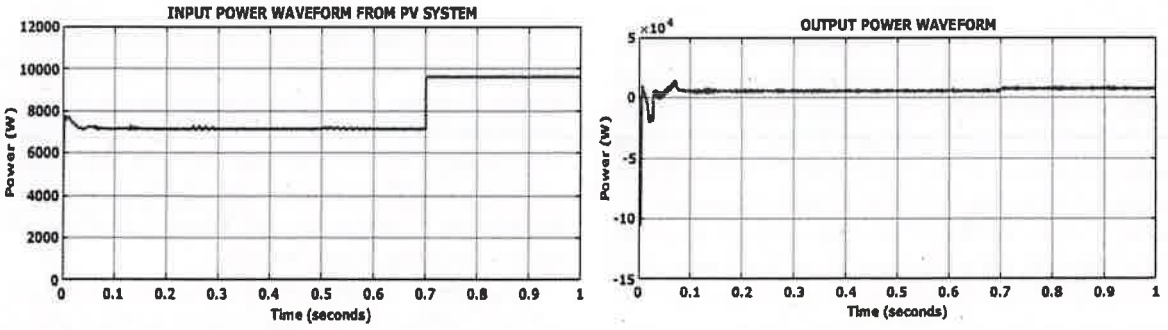

Fig. 18 Input and output power waveform from PV system

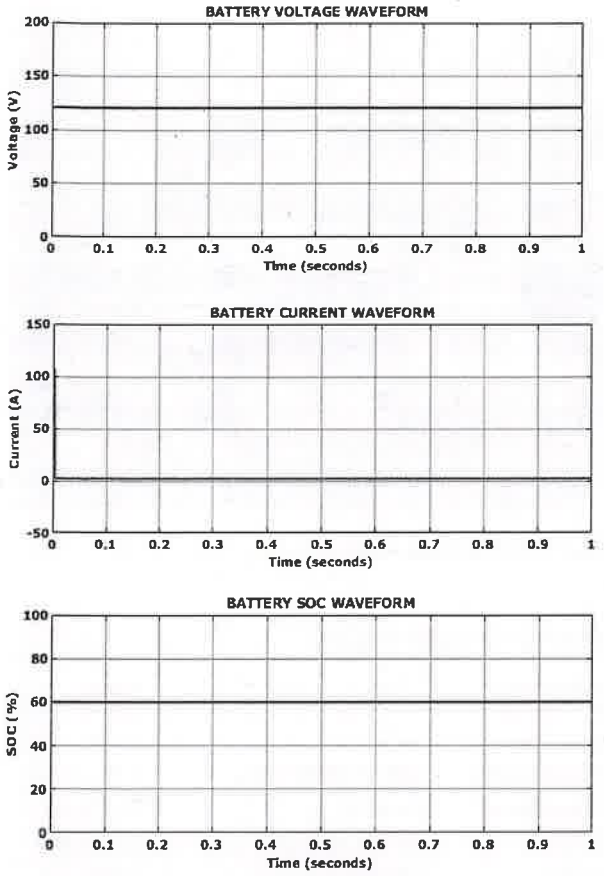

Fig. 19 Operational characteristics of battery waveforms

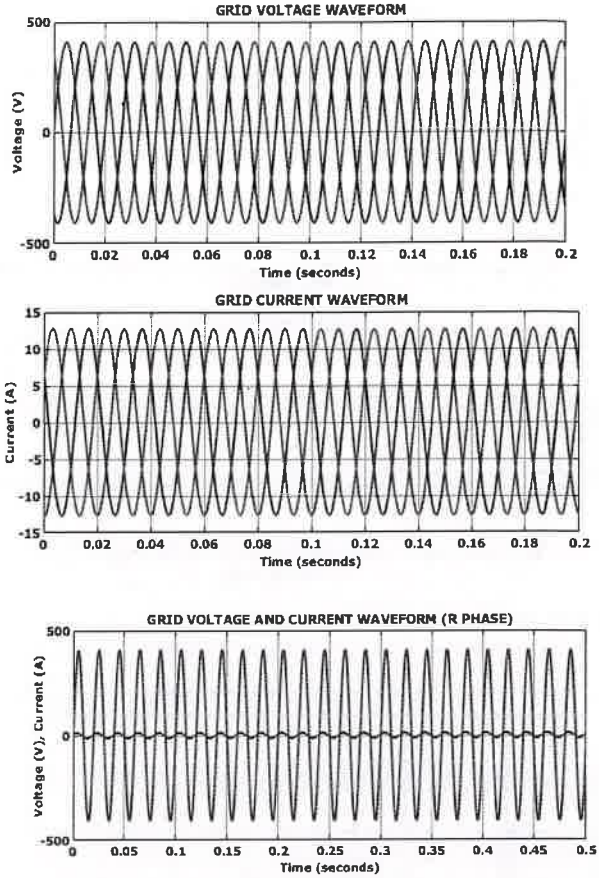

Fig. 20 Output waveforms of grid side

process the grid current waveform might show irregularities corresponding to the initial mismatch. By using a PI controller for grid synchronization involves adjusting the inverter output to equal the voltage in frequency, phase and amplitude. The waveforms before synchronization show phase differences and irregularities, which gradually diminish during the synchronization process. Once synchronized, the voltage and current waveforms become smooth and aligned, ensuring efficient and stable power transfer between the inverter and the grid. The PI controller plays a crucial role in minimizing the phase error and achieving stable synchronization.

Figure 21 denotes the output waveforms of 3ϕ inverter voltage using with and without filter. The voltage waveform is distorted and not a smooth sinusoid while without LC filter. In contrast, when a filter, typically an LC filter is employed, the high-frequency switching pulses are smoothed out, resulting in a more sinusoidal voltage waveform. The filtered voltage closely approximates a pure sine wave, significantly reducing harmonic content and high-frequency noise. Figure 22 denotes the real and reactive power of the grid side, it is observed that the stabilized actual and reactive power value is accomplished.

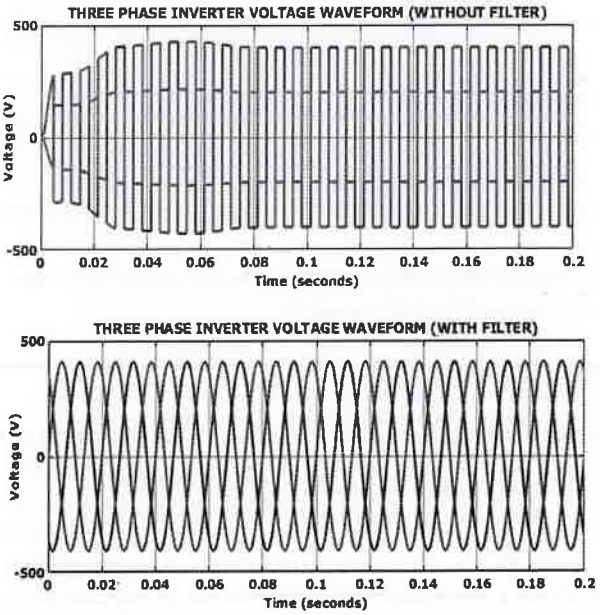

Fig. 21 Output waveforms of 3ϕ inverter voltage using with and without filter

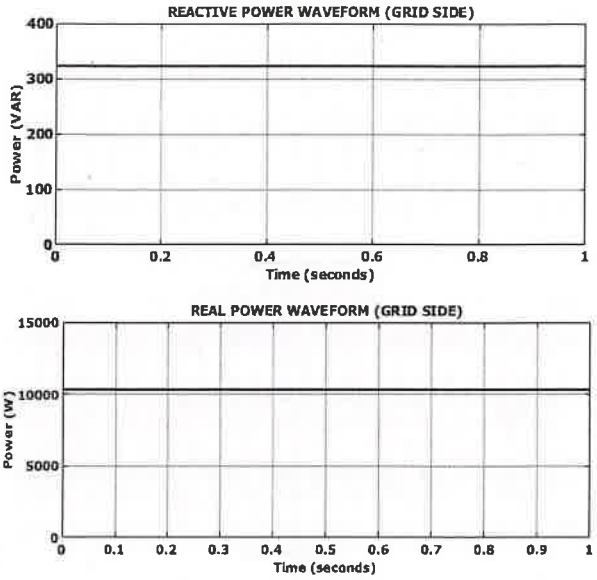

Fig. 22 Output waveforms of real and reactive power

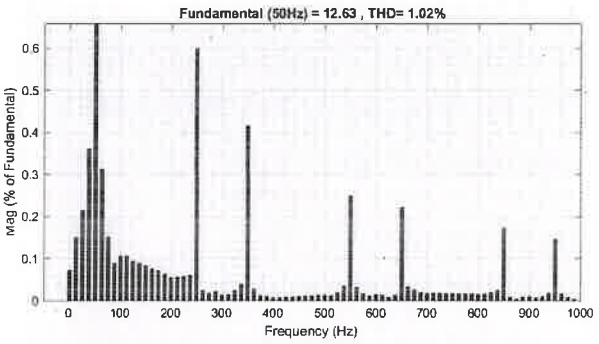

Fig. 23 THD waveform

Figure 23 demonstrates the proposed research THD waveform using HFA-SSO-tuned PI controller. With the use this optimized PI controller, the proposed work accomplishes the minimized THD value of 1.02%, which is fulfils the requirements of the IEEE-519 standard.

4.4 Hardware analysis

To assess the experimental evaluation of proposed PV-Grid system performance, the experimental setup is developed in collaboration with SPARTAN 6E FPGA microcontroller as seen in Fig. 24. The proposed work hardware components with their values are tabulated in Table 4, which includes the solar panel, microcontroller, driver circuit, switch and diode. To validate the functionality and performance of the proposed PV-Grid system, experimental testing has been conducted using the same converter parameters that were examined in the simulation study. This alignment between simulation

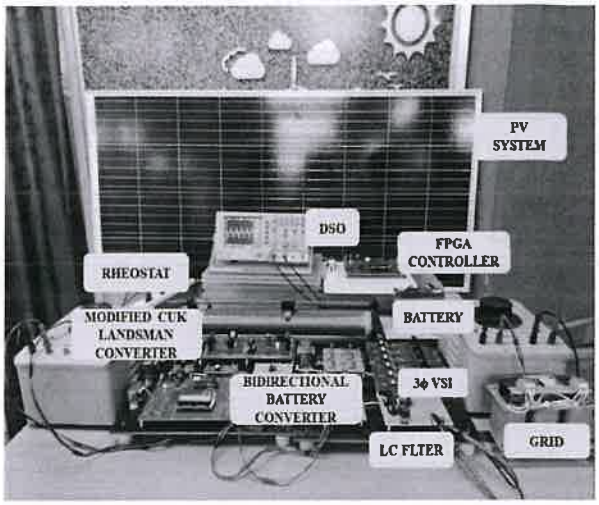

Fig. 24 Hardware setup image

Table 4 Hardware Specifications

Components	Type	Range
Solar panel	–	$1KW$
Microcontroller	SPARTAN 6E FPGA	$3.3V$
Driver Circuit	TLP250	$35V$, $1.5A$
Switch	STGW40H120F2, IGBT	$1200V$, $80A$
Diode	IN4007	$1000V$, $1A$

and experimentation allows for a meaningful comparison, verifying that the system behaves as expected under similar conditions. By using identical values for the converter, the consistency in results strengthens the reliability of the proposed design and ensures its practical viability for real-world PV-grid applications.

The solar module experimental output waveform of voltage and current is depicted in Fig. 25. It is proved that solar module maintain the consistent voltage, likewise, the solar module current value becomes constant with minor fluctuations. By examining the voltage waveform, it is evident that the solar module maintains a stable output voltage, reflecting the module's ability to provide a consistent energy supply. This stability is crucial for applications requiring reliable voltage levels, especially when integrated into larger energy systems like grid-connected PV systems.

The output voltage and current waveforms obtained employing Modified Cuk-Landsman DC to DC converter are showcased in Fig. 26. Here, the consistent converter voltage and current values are attained by using HFA-SSO-tuned PI controller. Additionally, it contributes to a faster settling time, meaning the system reaches a steady operating point more quickly after any perturbations or changes in input, thereby

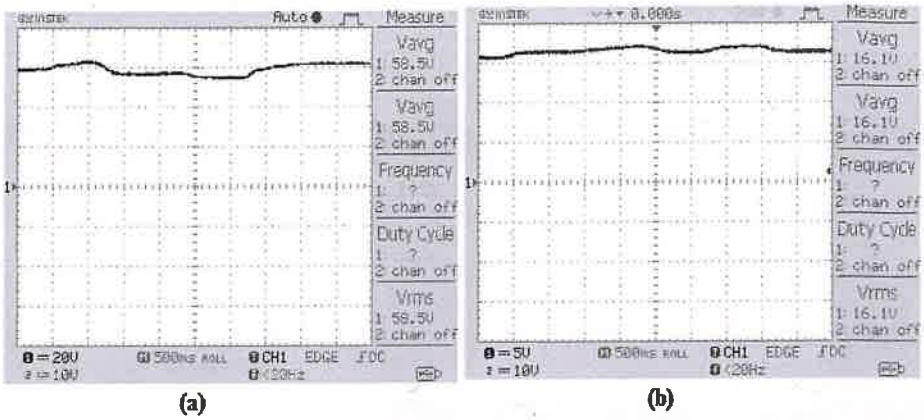

Fig. 25 Output Waveforms of Solar Module **a** Voltage **b** Current

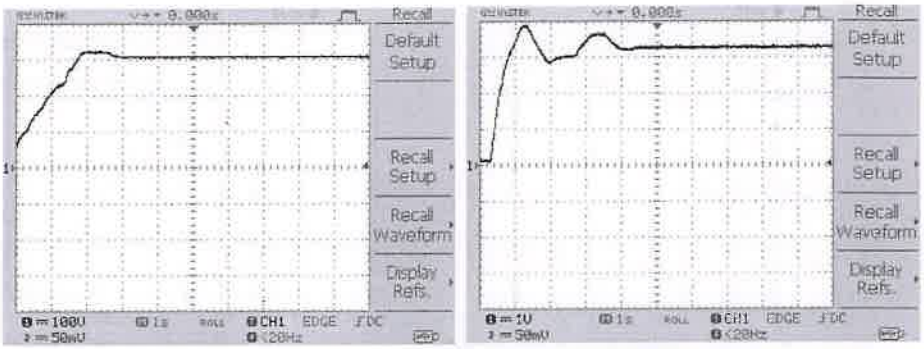

Fig. 26 Output Waveforms of Modified Cuk-Landsman Converter **a** Voltage **b** Current

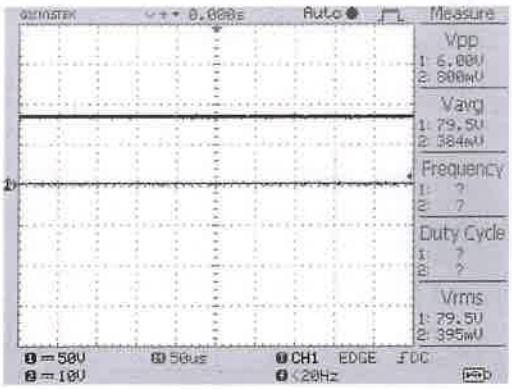

Fig. 27 Output waveform of battery SoC

enhancing the overall responsiveness and efficiency of the converter in maintaining desired output levels.

The SoC is a percentage-based measurement of the amount of energy accessible in a battery at a given time. Figure 27 shows that the battery SoC is 60% maintained. Figure 28 illustrates the three-phase grid voltage and current output profile. By switching the DC input voltage from the proposed converter, the 3ϕ VSI generates AC voltage. Similarly, the control technique and load impedance influence the VSI current waveform. The LC filter is utilized in the created system scenarios to reduce the harmonics generated by nonlinear loads.

The proposed research yields a THD value of 2.61%, as shown in Fig. 29, which is the amount of distortion observed in the proposed system. Table 5 compares the developed converter topologies with other converter topologies comparison in terms of voltage gain and efficiency, the developed system attains highest efficiency value of 96.8% with enhance voltage gain ratio as seen in Fig. 30.

The K_p, K_i values of proposed controller with other controllers like FA-PI and SSO-PI is denoted in Table 6. According to the table observation, it is clear that the proposed controller approach outperformed the others with regard to Integral Absolute Error (IAE) and Integral of Square Error (ISE).

Table 7 represents the comparison of dynamic responses of proposed HFA-SSO-tuned PI controller with other controller approaches including PI, PSO-PI, FA-PI and SSO-PI. According to the table outcomes, it is proved that the proposed controller approach has improved outcomes regarding settling time (0.1 s), overshoot (0.098%) and steady-state error (0.084).s

The convergence performance of proposed optimization algorithm comparison is provided in Fig. 31. This graph clearly proves that the proposed HFA-SSO algorithm has

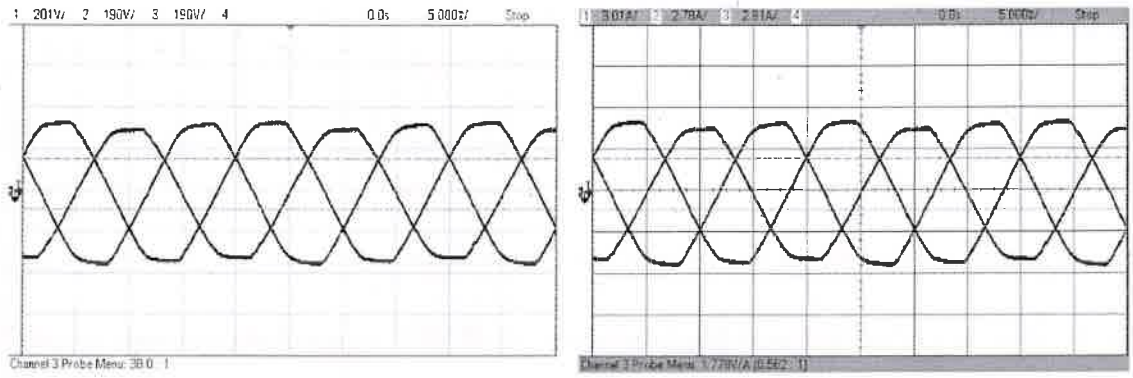

Fig. 28 Output waveform of grid side (Voltage and Current)

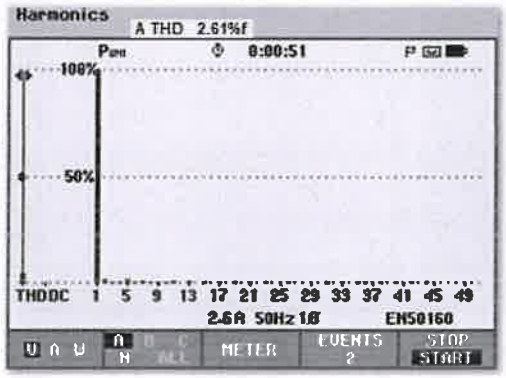

Fig. 29 THD

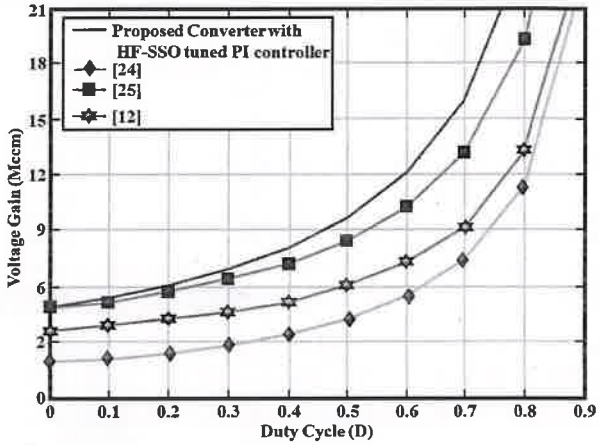

Fig. 30 Voltage gain comparison

Table 5 Comparison of Converter Performance Metrices

Converters	Components count					Voltage gain	Efficiency (%)
	S	D	L	C	CIC		
Converter in [24]	1	5	3	3	Yes	$\frac{D^2}{(1-D)^2}$	90%
Converter in [25]	2	2	2	2	No	$\frac{2(1+D)}{1-D}V_{in}$	91%
Converter in [12]	1	2	2	3	Yes	$\frac{1+D}{1-D}V_{PV}$	92.2%
Proposed Converter with HFA-SSO-PI controller	1	3	4	3	Yes	$\frac{D}{(1-D)^2}V_{PV}$	96.8%

$S \rightarrow$ Switch, $D \rightarrow$ Diode, $L \rightarrow$ Inductor, $C \rightarrow$ Capacitor, $CIC \rightarrow$ Continuous input current

Table 6 Optimized PI parameters

Optimized controller	Proportional gain (K_p)	Integral gain (K_i)	Level of output	
			ISE	IAE
FA-PI	0.3	0.05	3.36	2.45
SSO-PI	0.5	0.09	2.45	1.94
HFA-SSO-PI	0.25	0.0025	0.98	0.84

quick convergence speed in contrast to other optimization approaches. The employment of modified Cuk-Landsman converter along with HFA-SSO-tuned PI controller, the proposed system accomplishes minimized THD value of 1.02% when compared to other converter topologies as seen in Table 8.

Table 7 Dynamic response comparison of optimized PI controllers

Controller approach	Rise time (T_r)	Peak time (T_p)	Settling time (T_s)	Overshoot (%)	Steady-state error(%)
PI	0.2	0.4	0.4	1.235	2.68
PSO-PI	0.3	0.45	0.32	1.156	2.04
FA-PI	0.35	0.39	0.25	1.094	1.98
SSO-PI	0.24	0.21	0.15	0.985	1.45
HFA-SSO-PI (Proposed)	0.09	0.08	0.1	0.098	0.084

5 Conclusion

This research provides a novel method that combines a hybrid PI controller strategy with a modified Cuk-Landsman converter to enhance the performance of grid-connected PV system. The Modified Cuk-Landsman converter is employed to optimize power transfer and maximize efficiency by efficiently increasing the PV panels' output voltage. Using an HFA-SSO adjusted PI controller that combines Firefly and Swallow Swarm approaches is utilized to fine-tune the PI controller's parameters, the switching function of this converter is significantly improved. When it comes to controlling the PV system's power output, this optimized PI controller exhibits improved dynamic response and robustness. Additionally, a bidirectional DC-DC converter is integrated to guarantee steady battery voltage stabilization and efficient power management. By facilitating effective charging and discharging processes, this converter preserves battery performance and lengthens its lifespan. To provide precise and dependable integration of the PV system with the grid, an effective grid synchronization technique called a RNN controller is utilized. From the obtained simulation and experimental outcomes, is it proved that the proposed work attains improved results with regard to voltage gain, efficiency (96.8%) with minimized THD value of 1.02%. The implications of this research for real-world applications are significant, particularly for the integration of sustainable energy sources into existing power grids. By introducing a Modified Cuk-Landsman converter alongside a hybrid PI controller strategy, this system effectively addresses common challenges in grid-connected PV systems, such as achieving stable and optimal power transfer. For practical implementation, this system presents promising compatibility with existing grid structures. The RNN controller aids in smooth grid synchronization, enabling accurate and stable integration with minimal risk of power inconsistencies. This feature makes the proposed approach suitable for real-world applications where fluctuations in solar energy can impact grid stability. However, challenges could arise during implementation, particularly related to the complexity of optimizing

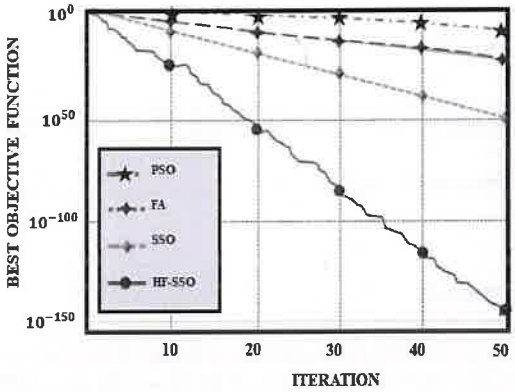

Fig. 31 Convergence speed comparison

Table 8 THD comparison

Methodologies	THD (%)
Boost converter	4.25
Cuk converter	3.68
Landsman converter	2.46
Modified Cuk-Landsman converter with HFA-SSO-PI	1.02

the parameters of the PI controller and ensuring the RNN-based synchronization can adapt to various grid conditions in different regions. Another potential challenge could be the cost and complexity associated with implementing advanced optimization techniques (HFA-SSO) in existing infrastructures. Nevertheless, with adequate testing and calibration, the proposed system is adapted to integrate smoothly, making it a viable and effective solution for enhancing PV-grid connectivity and supporting sustainable energy initiatives.

5.1 Limitations and future directions

The system's performance under extreme environmental conditions and scalability for larger PV setups are not fully addressed. Future directions involve developing adaptive control strategies for real-time operation, integrating IoT

and smart grid technologies for enhanced monitoring, and exploring advanced control methods to improve robustness and scalability.

Author's contributions Conceptualization: EI. Data Curation: EI. Methodology: RM and EI. Project administration: RM. Supervision: RM. Validation: RM. Writing—original draft: EI. Writing—review and editing: RM and EI.

Funding The authors received no specific funding for this study.

Availability of data and materials No datasets were generated or analyzed during the current study.

Declarations

Conflict of interest An authors have no conflicts of interest to declare that are relevant to the content of this article.

Ethics approval Not applicable.

References

1. Kavin KS, Subha Karuvelam P, Devesh Raj, M, Sivasubramanian M (2024) A novel KSK converter with machine learning MPPT for PV applications. Electric Power Comp Syst, pp 1–19.
2. Tawfiq AA, El-Raouf MO, Mosaad MI, Gawad AF, Farahat MA (2021) Optimal reliability study of grid-connected PV systems using evolutionary computing techniques. IEEE Access 9:42125–42139
3. Rahman S, Saha S, Islam SN, Arif MT, Mosadeghy M, Haque ME, Oo AM (2021) Analysis of power grid voltage stability with high penetration of solar PV systems. IEEE Trans Ind Appl 57(3):2245–2257
4. Dhibi K, Mansouri M, Bouzrara K, Nounou H, Nounou M (2021) An enhanced ensemble learning-based fault detection and diagnosis for grid-connected PV systems. IEEE Access 9:155622–155633
5. Ali MN, Mahmoud K, Lehtonen M, Darwish MM (2021) An efficient fuzzy-logic based variable-step incremental conductance MPPT method for grid-connected PV systems. IEEE Access 9:26420–26430
6. Inomoto RS, De Almeida Monteiro JR, Sguarezi Filho AJ (2022) Boost converter control of PV system using sliding mode control with integrative sliding surface. IEEE J Emerg Selected Top Power Electronics 10(5):5522–5530
7. Guerra MI, Ugulino de Araújo FM, Dhimish M, Vieira RG (2021) Assessing maximum power point tracking intelligent techniques on a PV system with a buck–boost converter. Energies 14(22):7453
8. Janarthanan SK, Kathirvel C (2022) Optimized CUK converter based 1Φ grid tied photovoltaic system. Intell Autom Soft Comput 34(1):33–50
9. Hasanpour S, Forouzesh M, Siwakoti YP, Blaabjerg F (2021) A new high-gain, high-efficiency SEPIC-based DC–DC converter for renewable energy applications. IEEE J Emer Selected Top Ind Electronics 2(4):567–578
10. Joshi K, Raut V, Waghmare S, Waje M, Patil RM (2022) Maximum power operation of a PV system employing zeta converter with modified P&O algorithm. Int J Eng Trends Technol 70(7):348–354
11. Anbarasan P, Venmathi M, Vijayaragavan M, Krishnakumar V (2022) Performance enhancement of grid integrated photovoltaic system using luo converter. IEEE Can J Electrical Comput Eng 45(3):293–302
12. Karthikeyan M, Elavarasu R, Ramesh P, Bharatiraja C, Sanjeevikumar P, Mihet-Popa L, Mitolo M (2020) A hybridization of cuk and boost converter using single switch with higher voltage gain compatibility. Energies 13(9):2312
13. Rezvanyvardom M, Mirzaei A (2020) High gain configuration of modified ZVT SEPIC-Boost DC-DC converter with coupled inductors for photovoltaic applications. Sol Energy 208:357–367
14. Bhaskar MS, Gupta N, Selvam S, Almakhles DJ, Sanjeevikumar P, Ali JS, Umashankar S (2021) A new hybrid zeta-boost converter with active quad switched inductor for high voltage gain. IEEE Access 9:20022–20034
15. Mahdizadeh S, Gholizadeh H, Gorji SA (2022) A power converter based on the combination of Cuk and positive output super lift Lou converters: circuit analysis, simulation and experimental validation. IEEE Access 10:52899–52911
16. Aourir M, Abouloifa A, Lachkar I, Aouadi C, Giri F, Guerrero JM (2020) Nonlinear control and stability analysis of single stage grid-connected photovoltaic systems. Int J Electr Power Energy Syst 115:105439
17. Naidu TA, Arya SR, Maurya R, Padmanaban S (2021) Performance of DVR using optimized PI controller based gradient adaptive variable step LMS control algorithm. IEEE J Emerg Selected Top Ind Electronics 2(2):155–163
18. Fodil M, Djerioui A, Ladjal M, Saim A, Berrabah F, Mekki H, Zeghlache S, Houari A, Benkhoris MF (2023) Optimization of PI controller parameters by GWO algorithm for five-phase asynchronous motor. Energies 16(10):4251
19. Mosaad MI (2020) Whale optimization algorithms-based PI controllers for renewable hybrid power system. World J Modell Simul 16(1):26–40
20. Ahmad A, Kashif SA, Nasir A, Rasool A, Liaquat S, Padmanaban S, Mihet-Popa L (2021) Controller parameters optimization for multi-terminal DC power system using ant colony optimization. IEEE Access 9:59910–59919
21. Abdolrasol MG, Hannan MA, Hussain SS, Ustun TS (2022) Optimal PI controller based PSO optimization for PV inverter using SPWM techniques. Energy Rep 8:1003–1011
22. Litwin M, Zieliński D, Gopakumar K (2020) Remote micro-grid synchronization without measurements at the point of common coupling. IEEE Access 8:212753–212764
23. Elnozahy A, Yousef AM, Abo-Elyousr FK, Mohamed M, Abdelwahab SA (2021) Performance improvement of hybrid renewable energy sources connected to the grid using artificial neural network and sliding mode control. J Power Electronics 21:1166–1179
24. Zhang N, Zhang G, See KW, Zhang B (2018) A single-switch quadratic buck-boost converter with continuous input port current and continuous output port current. IEEE Trans Power Electron 33:4157–4166
25. Farsizadeh H, Gheisarnejad M, Mosayebi M, Rafiei M, Khooban MH (2020) An intelligent and fast controller for DC/DC converter feeding CPL in a DC microgrid. IEEE Trans Circuits Syst II Express Br
26. Singh JK, Al Jaafari K, Behera RK, Al Hosani K, Muduli UR (2022) Faster convergence controller with distorted grid conditions for photovoltaic grid following inverter system. IEEE Access 10: 29834–29845
27. Madaria, Pankaj Kumar, Mohit Bajaj, Surbhi Aggarwal, and Amit Kumar Singh. "A grid-connected solar PV module with autonomous power management." In 2020 IEEE 9th power India international conference (PIICON), pp. 1–6. IEEE, 2020.
28. Abdel-Rahim O, Wang H (2020) A new high gain DC-DC converter with model-predictive-control based MPPT technique for photovoltaic systems. CPSS Transactions on Power Electronics and Applications 5(2):191–200
29. Rajagopal V, Sharath D, Vishwas G, Bangarraju J, Arya SR, Venkatesh C (2022) Optimized controller gains using grey wolf

algorithm for grid tied solar power generation with improved dynamics and power quality. Chinese J Electrical Eng 8(2):75–85
30. Mansor MA, Hasan K, Othman MM, Noor SZBM, Musirin I (2020) Construction and performance investigation of three-phase solar PV and battery energy storage system integrated UPQC. IEEE Access 8:103511–103538